ELSEVIER

Journal of Chromatography A, 942 (2002) 249–258

JOURNAL OF CHROMATOGRAPHY A

www.elsevier.com/locate/chroma

Contactless conductivity detection for capillary electrophoresis Hardware improvements and optimization of the input-signal amplitude and frequency

José A. Fracassi da Silva[a], Norberto Guzman[b], Claudimir L. do Lago[a,*]

[a]*Departamento de Química Fundamental, Instituto de Química, Universidade de São Paulo, Av. Prof. Lineu Prestes 748, CEP 05508-900, São Paulo (SP), Brazil*

[b]*R.W. Johnson Pharmaceutical Research Institute, 1000 Route 202, Box 300, Raritan, NJ 08543, USA*

Received 14 May 2001; received in revised form 28 August 2001; accepted 9 October 2001

Abstract

A new prototype of contactless conductivity detector, smaller and easier to operate than the former version, is described. For a fused-silica capillary with 142-μm wall thickness and voltages up to 25 kV, it can be placed at the low- or high-voltage end of the column. This feature allowed implementation of an apparatus with sample introduction at the grounded end of the column. The input signal is an important parameter for determining the signal-to-noise ratio (S/N) of the detection system. An optimization procedure of its amplitude and frequency is proposed. Although the S/N must be determined by introduction of actual samples, the operating conditions can be optimized merely by changing the signal parameters and by using a mathematical procedure. Thus, an easy and fast optimization routine can be carried out. Mathematical and instrumental backgrounds are discussed, and experimental support of the technique's effectiveness is presented.

Keywords: Conductivity detection; Detection, electrophoresis; Instrumentation; Metal cations

1. Introduction

Since its introduction to capillary zone electrophoresis (CZE), conductivity detection (CD) has demonstrated great potential in the field of ion analysis [1,2]. CD provides a good alternative to photometric detection, principally in the low concentration range, when the lack of sensitivity is the major drawback for indirect ultraviolet detection.

A large number of ionic compounds have been separated and analyzed using CZE with CD. In part, this was made possible by the introduction of commercial CE equipment provided with CD [3,4]. Anions have been quantified in different matrices, such as beverages [5–7], environmental samples [8–13], electrodeposition coatings [14–16], and hydrogen peroxide [17]. Transient isotachophoresis (ITP) [18] and ITP–CZE [19] proved to be suitable methods for trace inorganic anion analysis. Surfactants have been separated and detected indirectly [20,21]. Bacterial sulfur degradation has been characterized by the analysis of sulfur-containing anions with both ion chromatography and CE [22]. Inorganic ions were quantified in rat lung airway surface fluid [23]. Williams and Boucher [24] performed the

*Corresponding author. Fax: +55-11-815-5579.

E-mail address: claudemi@iq.usp.br (C.L. do Lago).

0021-9673/02/$ – see front matter
PII: S0021-9673(01)01380-2

analysis of potassium counter ion and cation impurities in drug substances, and Stocking et al. [25] determined alkaline, earth alkaline, and ammonium from renal tubules in vivo. Also, CD was used in the determination of monoamine mobilities [26], and in the characterization of flow modifiers [27].

Important steps in the development of instrumentation for CE with CD involve the construction of suppressed systems [28–31] and new cell and circuit designs [32–35]. Theoretical considerations include running buffer optimization [36], calibration [37], and prediction of zone patterns [38].

Recently, contactless conductivity detection (CCD) or oscillometric detection (OD) has gained attention as an alternative to conventional conductometric measurements. In this case, a high-frequency alternate signal is applied to one or two electrodes in the detector cell. As the capacitive reactance diminishes with the increase in frequency, the capillary impedance is reduced, and good signal variations can be observed with the electrodes positioned outside the capillary. This arrangement prevents electrode contamination and interferences from the separation electric field.

Zemann et al. [39] and Silva and Lago [40] first described prototypes of CCD and OD for CZE, operating at 20 or 40 kHz and 600 kHz, respectively. The influence of the internal diameter of the capillary on the response of the detector was considered by Mayrhofer et al. [41]. Gas et al. [42] and Vacík et al. [43] applied to CZE a previous contactless detector originally designed for ITP. Kaniansky et al. [44] evaluated the response characteristic, short-term noise, and detection sensitivity. The same group also used the system for the detection of anions using α-cyclodextrin to promote separation [45], and in the characterization of purities of alkyl- and arylamino derivatives of β-cyclodextrin [46]. Silva and Lago [47] used OD for the detection of aliphatic alcohols separated by micellar electrokinetic chromatography (MEKC). Recently, Chvojka et al. propose a combined system with simultaneous contactless conductivity and photometric detection [48].

Although CCD and OD are essentially conductivity detection, there are particularities imposed by the presence of the capillary wall, the cell geometry, and electronics. Thus, it is important that some effort is made to understand, improve, and optimize the technique in order to confirm it as practical and useful. In this work, some hardware improvements are described and optimization of the input signal is discussed.

2. Experimental

2.1. Contactless conductivity detector

A block diagram of the detector circuit is shown in Fig. 1. Two electrodes are positioned over the capillary. A sinusoidal potential provided by a function generator is imposed over one of these electrodes. The other electrode is connected to a current-to-voltage converter. The alternating current signal is then rectified, filtered, amplified, and baseline compensated. This new circuit has basically the same design as the previous one [40], but the rectifying step was included in module 1 and a buffer was included as a first step in module 2. An OPA2604AU dual operational amplifier (Burr Brown, Tucson, AZ, USA) performs the two initial steps in module 1, and an OPA2604AP is used in module 2.

Module 1 was implemented using a surface-mount

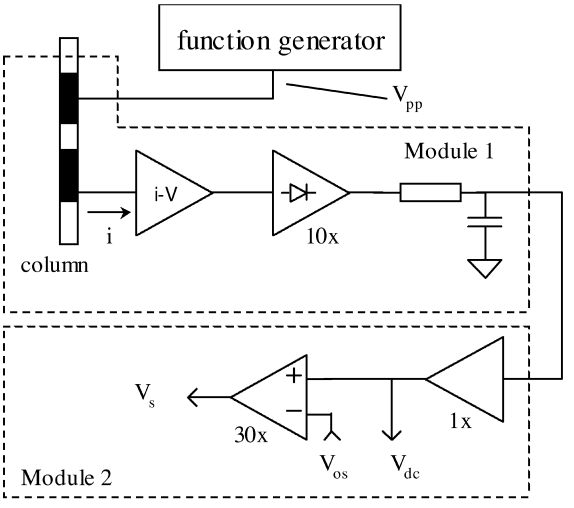

Fig. 1. Contactless conductivity detector block diagram. Rectifier, buffer, and final amplifier have gains of 10, 1, and 30, respectively. The feedback resistor in the current-to-voltage converter is 1 MΩ.

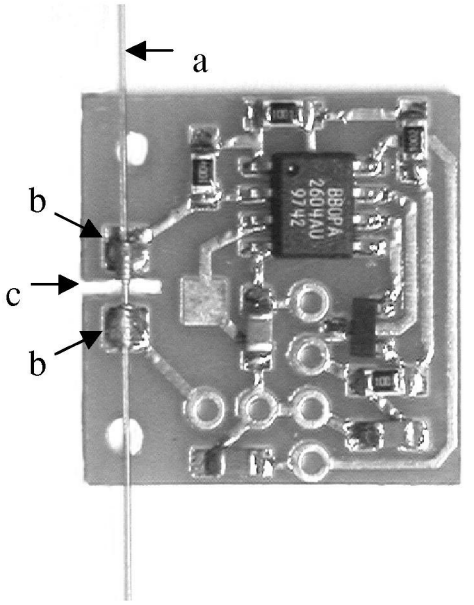

Fig. 2. Module 1 printed circuit board: (a) fused-silica capillary column, (b) tubular electrode, (c) air gap. Connections from the function generator and module 2 were not made. Silicone rubber cover and metallic shield are not shown.

device (SMD) technique, resulting in an 18×18-mm printed circuit board (Fig. 2). The board comprises not only the electronic circuit, but also the cell. The cell electrodes are soldered directly onto the circuit pads. The board region between these pads is cut to render a 0.7-mm air gap between the 2-mm long electrodes.

Module 1 is covered by RTV silicone rubber (Profor, Diadema, SP, Brazil). After the silicone is cured, the block is placed inside a grounded metal shielding. Fig. 2 shows the circuit before the silicone rubber is applied.

The electrodes were fabricated by a wire-wrapping technique used to assemble an electronic circuit prototype. A stainless steel needle with the same capillary outer diameter is used as a support for wrapping the uncovered wire. The number of spirals determines the length of the electrode. To prevent inductive behavior, the resulting spirals must be tied in. Before removing the coil of the support, tin-lead solder is applied over the spirals. The resulting tubular electrodes are then aligned and soldered onto the printed circuit board, as show in Fig. 2.

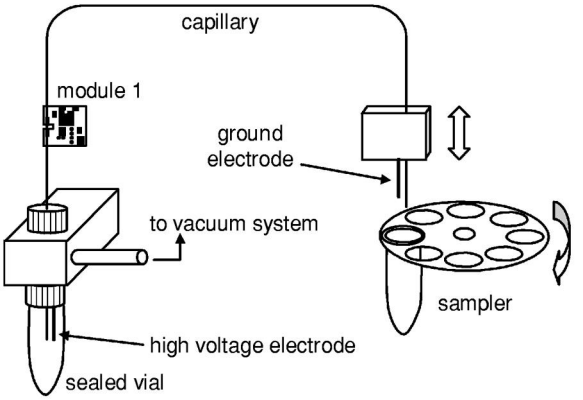

Fig. 3. Block diagram of the CE apparatus. Module 1 is positioned ~8 cm from the high-voltage capillary end. The high-voltage electrode vial is sealed in order to prevent electrical discharges and allow hydrodynamic injection.

2.2. CE apparatus

Fig. 3 is a simplified diagram of the apparatus, which comprises a thermostated plexiglas case, a 50 cm×75 μm I.D.×360 μm O.D. fused-silica capillary (J&W Scientific, Folsom, CA, USA), an eight-vial automatic sampler, a sealed vial with the high-voltage electrode, two interchangeable 0–30-kV power supplies (models R15-30P and R15-30N, Matsusada, Japan) for positive and negative voltages, respectively, and the contactless conductivity detector positioned at the high-voltage side. The sinusoidal signal with adjustable amplitude and frequency was produced by a FG-2002C function generator (Goldstar, South Korea). The data acquisition system was described previously [40]. Data treatment was performed in Microcal Origin 5.0 (Microcal Software, Northampton, MA, USA) and Mathcad 8.0 (MathSoft, Cambridge, MA, USA).

2.3. Solutions and reagents

All solutions were prepared with Nanopure (Barnstead, Iowa, USA) deionized water and all the chemicals were reagent or analytical grade and used as received. Sample solutions with alkaline and earth-alkaline cations were prepared by diluting 100 m*M* stock solutions of KCl, NaCl, $BaCl_2$, and LiCl, and a final concentration of 100 μ*M* was given in

each cation. Sample solutions with sulfate, methanesulfonate, and lactate (Lac) were prepared by diluting 100 m*M* stock solutions of Na_2SO_4, CH_3SO_3H, and sodium lactate, and a final concentration of 100 μ*M* was given in each anion For cation and anion analyses the running buffers were 20 m*M* histidine–lactate (His/Lac) (pH 4.9) and 20 m*M* 2-(*N*-morpholino)ethanesulfonic acid–histidine (MES/His) with 0.2 m*M* cetyltrimethylammonium bromide (pH 6.0), respectively.

3. Results and discussion

3.1. Improvements to the detector and equipment

In the previous version of this detector [40], a ground plane was placed between the electrodes to minimize the direct transmission of the signal.

Subsequently, Mayrhofer et al. [41] also added this ground plane to their cell. However, we observed that this plane did not significantly improve the signal-to-noise ratio (*S*/*N*). Moreover, by removing this plane, the amplitude of the applied sinusoidal signal could be reduced without significant loss of performance. In the version of the detector with the ground plane, the limits of detection estimated for K^+, Na^+, Li^+, Ca^{2+}, Ba^{2+}, and Mg^{2+} were ~1–2 μ*M* [40]. For the same experimental condition (including the operating frequency), the new detector gives about the same limits of detection (LODs) with V_{pp} equal to 2 V instead of 20 V.

During performance tests of the detector, we were able to identify a significant effect of the ambient temperature over module 1. Since the operational amplifier has as low an offset-voltage drift as the previous one, this effect is not expected. The main cause seems to be the low thermal capacity of the components due to the small size of the SMD parts and the convective airflow inside the case. Thus, to overcome this problem, module 1 circuit was immersed in silicone rubber. The region of the printed circuit board, where the column and electrodes are positioned, was kept outside the silicone rubber.

In the first version of the detector, the electrodes were made of silver paint. Although this paint renders good electrical contact with the column, the mechanical resistance is poor and replacement of the column is troublesome. Zemann et al. [39] have used stainless steel needles as the electrodes, because the column can easily slide inside them. However, the gap between the inner surface of the needle and the external surface of the capillary adds a new capacitor in series with that represented by the fused-silica wall. Although the air gap is significantly thinner than the silica wall size, it is an important component because the permittivity of the silica is about three times greater than the permittivity of the air. Moreover, the mobility of the column may introduce variations in the dielectric thickness of the air gap, which results in impedance variations and increasing noise. For long electrodes like those used by Zemann et al., the effect of the air gap may not be significant, but for short electrodes, it diminishes the performance. We tried to fit the inner diameter of a small-bore needle to the outer diameter of the capillary by acid corrosion. However, controlling the corrosion process to obtain the correct diameter is laborious. A better alternative is to fabricate the electrode with the wire-wrapping technique described in the Experimental section. The resulting electrode does not provide the same contact as the silver paint, but it fits the silica capillary quite well. The same approach was used by Chvojka et al. [48].

In the early version of the equipment, the samples were introduced at the high-voltage capillary end and the detector was placed at the low-voltage side. This arrangement is always employed in electrochemical detection schemes. However, it is problematic for some hyphenated systems such as flow injection analysis–capillary electrophoresis (FIA–CE). Moreover, discrete samplers such the one shown in Fig. 3 can be more easily implemented when the sample is introduced at the low-voltage end, because the risk of an electrical discharge through the metallic parts is minimized. Thus, we decided to implement this configuration, which is, to the best of our knowledge, the first CE system with electrochemical detection at the high-voltage end.

Based on the electric discharge strength for silica (200 kV cm^{-1}) [49], the typical wall thickness of the column we used (142 μm) would prevent electric discharge up to 2.84 kV, which is not enough for actual CE systems. However, this electric strength holds for 5 mm or more in thickness, being higher for thinner walls [49]. In addition, the polyimide

coating extends the electric discharge strength of the wall. In practice, we have no problem up to 25 kV in continuous use. It is important also to consider that the detector is positioned at a few centimeters from the high-voltage end; thus the inner potential at the cell region is lower than the applied voltage.

3.2. Optimization of the contactless conductivity detector

At first glance, the higher the peak-to-peak voltage (V_{pp}), the higher the output signal must be. However, S/N does not necessarily follow the same trend, because the noise at the circuit output results from the combination of the noise at all individual parts. Moreover, the electronics used in module 1, which comprise the critical steps of the signal processing, have a limited capability to amplify small signals at high frequency. Therefore, a set of experiments was carried out in order to evaluate the influence of the amplitude and frequency of the input signal over the S/N.

In the following experiments, the baseline was evaluated at the V_{dc} point, and the noise at the V_s point. The signals were monitored for ~1 min. Since we are concerned with the noise due to the electronics, the long-term noise must be removed prior to its evaluation, because long-term noise is attributed to the other source, e.g. conductivity variations due to temperature changes. Thus, each signal sample was filtered using a high-pass fast Fourier transformer filter with a 1-Hz cut-off frequency. The noise was established as the standard deviation of the output voltage (σ_{Vs}).

Fig. 4 shows baseline and noise as a function of the operating frequency for different values of V_{pp}. In order to distinguish the contributions from the cell and circuitry to the V_s noise, a 10-MΩ resistor was substituted for the cell in this experiment. Because of the residual capacitance of this component and the natural leakage capacitance of the circuit board, a continuous increase in V_s as a function of the frequency is expected. However, due to the limitations of the real operational amplifiers, this is not observed. Fig. 4a shows that there is a maximum of the baseline and that this point is shifted to low frequencies for high V_{pp} values. Although the behavior of the noise is not as simple as the baseline, it

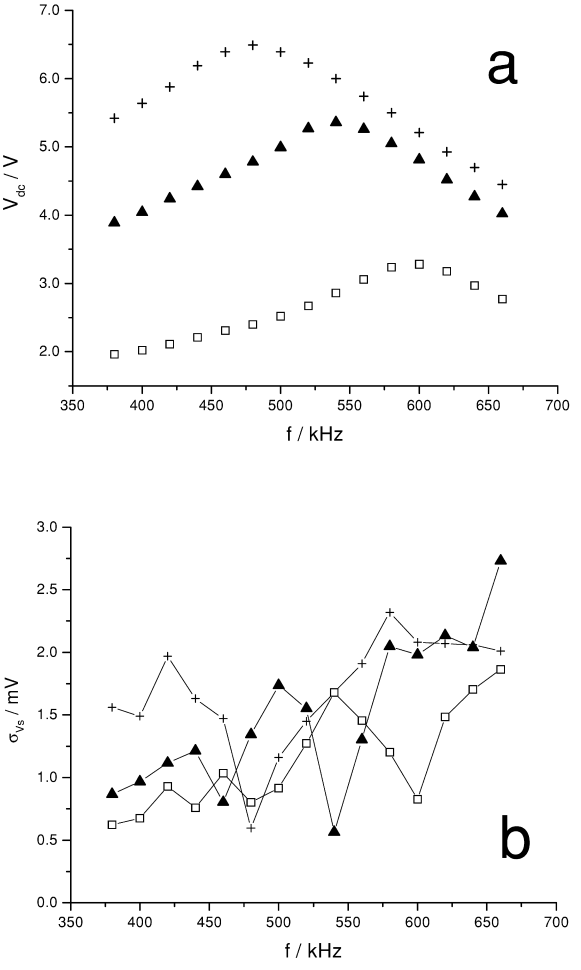

Fig. 4. Baseline (V_{dc}) and noise (σ_{Vs}) as a function of operating frequency at different V_{pp} values: (□) 2.0 V, (▲) 4.0 V, and (+) 6.0 V. The cell was substituted by a 10-MΩ resistor.

is possible to note a minimum point at the same frequency of the baseline maximum. This trend is observed not only with the resistor, but also when using the cell, and its origin is not well understood.

Fig. 5 shows the baseline and noise as a function of the V_{pp} at 400 and 590 kHz. From these curves, one can observe that the baseline varies linearly at low values of frequency and/or V_{pp} and there is a trend of the noise to rise with V_{pp}.

Fig. 6 shows electropherograms of the same sample at different values of frequency and amplitude (V_{pp}). These electropherograms should not be compared to those ones from the previous version of

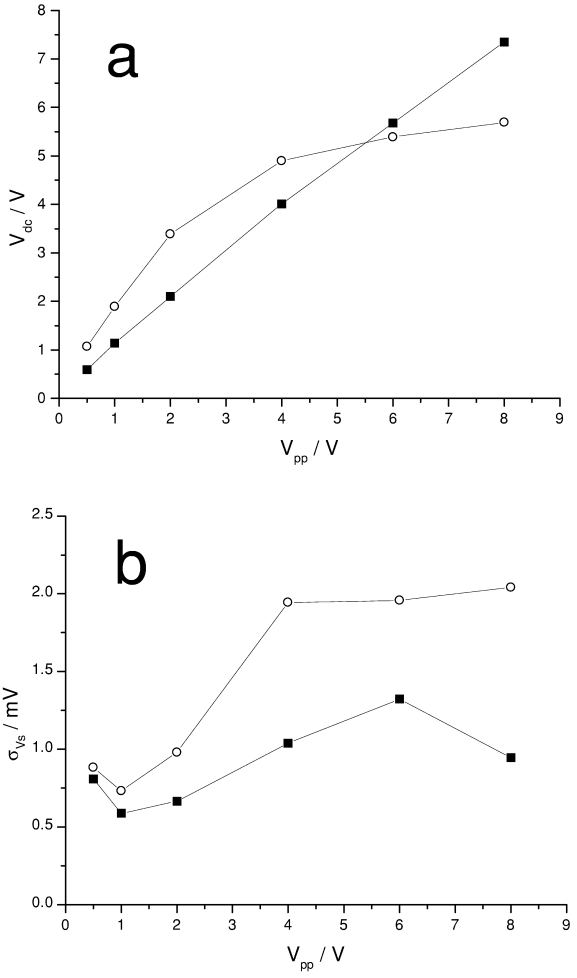

Fig. 5. Baseline (V_{dc}) and noise (σ_{Vs}) as a function of V_{pp} at different operating frequencies: (■) 400 kHz and (○) 590 kHz. The cell was substituted with a 10-MΩ resistor.

the detector [40], because different conditions were used in both cases. The running buffer was Lac/His that has a different performance on conductometric detection when compared to MES/His buffer that was used in the former work. Moreover, the volume of the injected sample, the length of the column, and temperature control are different. The electropherograms in Fig. 6 should be compared among themselves. They do not exemplify the best performance of the new system. On the contrary, they were selected because they emphasize the need for optimization.

At 400 kHz, the peak heights increase according

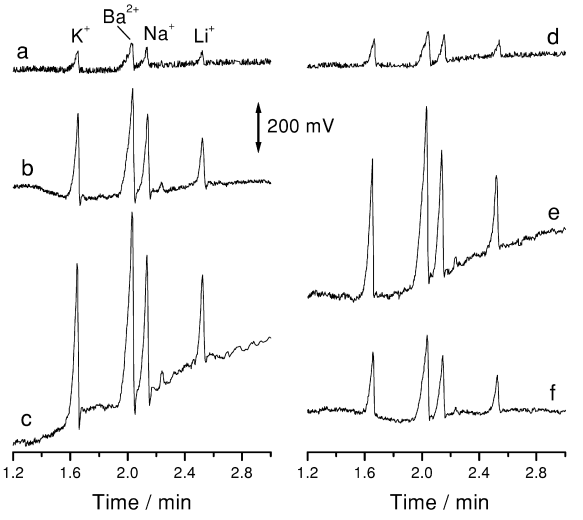

Fig. 6. Electropherograms of 100 μ*M* solution of K^+, Ba^{2+}, Na^+, and Li^+ in 20 m*M* Lac/His buffer. Pressure injection at 4 p.s.i. for 3 s (1 p.s.i. = 6894.76 Pa). Operating frequencies: (a), (b), and (c) at 400 kHz and (d), (e), and (f) at 590 kHz. Peak-to-peak voltages: (a) and (d) at 0.5 V; (b) and (e) at 3.0 V; (c) and (f) at 6 V.

to V_{pp}. On the other hand, at 590 kHz, when V_{pp} is augmented from 0.5 to 3 V, the peak heights increase, but decrease at 6 V. To understand this behavior, the following consideration must be taking into account.

An ideal operational amplifier has infinite bandpass, i.e. the circuit works in the same way at any frequency. However, an actual operational amplifier has limitations, among which is the non-constant output voltage swing as a function of the frequency. This means that, for a low-frequency signal, the operational amplifier is able to generate an output voltage limited only by the power supply. However, for a high-frequency signal, the output amplitude range is reduced. The operational amplifiers in module 2 are not affected, because the signal at its input is practically d.c. However, both module 1 operational amplifiers operate at high frequency. This effect leads to a non-linear response, as shown in Fig. 5.

The measured signal (V_s) is proportional to the ΔV_{dc}, which is a function of the current at module 1 input. This current is given by V_{pp} and the cell admittance. Thus, V_s is given by:

$$V_s = A\,\Delta V_{dc} = A[g(i_1, f) - g(i_0, f)] \quad (1)$$

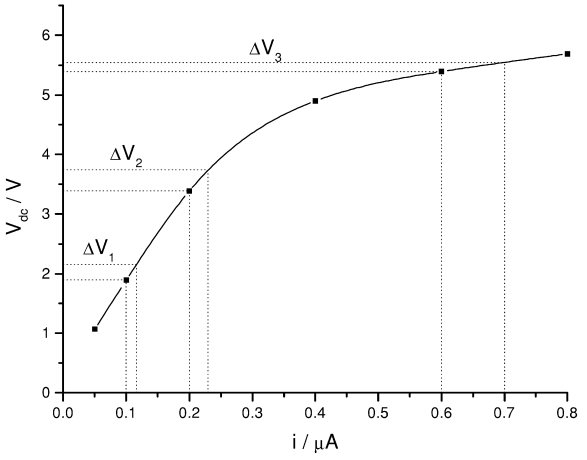

Fig. 7. Simulated baseline (V_{dc}) as a function of the input current. The same input stimulus (conductivity variation) gives different variations of current for different values of V_{pp}. Due to the non-linearity of the transfer function, the corresponding variation of V_{dc} is not proportional over the entire range. In this example, the larger variation of current (0.6–0.7 μA) gives the smaller variation of V_{dc} (ΔV_3).

where f is the operating frequency, $g(i,f)$ is a function that describes the shape of the curve from Fig. 7, and A is the gain of the last stage of module 2. The indexes 0 and 1 represent two different input conditions, e.g. at baseline and at the top of an electrophoretic peak, respectively. The following assertion considers that the frequency is held constant. Because V_s corresponds to small changes in V_{dc}, Eq. (1) can be approximated to:

$$V_s = A[i_1 - i_0]g'(i_0) \tag{2}$$

where $g'(i_0)$ is the derivative of $g(i)$ at the current i_0.

The consequence of this mathematical formulation may be best understood by a graphic demonstration. Fig. 7 shows three hypothetical conditions, in which the input currents are 0.1, 0.2, and 0.6 μA for the same cell admittance (same buffer conductivity) and three different values of V_{pp}. The same input stimulus (solution conductivity variation) will give different values of Δi. However, due to the non-linearity, the corresponding values of ΔV_{dc} do not follow the same trend as Δi, i.e. although ΔV_3 corresponds to the highest Δi, it is lower than ΔV_2. This clarifies the different sensitivities shown in the electropherograms in Fig. 6.

The current is the product of the cell admittance (Y) by the amplitude (V_{pp}). It is not easily determined, because, although V_{pp} is known, Y is not directly measured. A more suitable approach is the variable replacement:

$$V_s = \frac{A\,\Delta Y}{Y_0} \cdot V_{pp0} h'(V_{pp0}) \tag{3}$$

where the function h describes V_{dc} as a function of V_{pp} and V_{pp0} and Y_0 are the amplitude and cell admittance, respectively, at the baseline corresponding to i_0.

The S/N could be evaluated by:

$$SNR = \frac{A\,\Delta Y}{Y_0} \cdot \frac{V_{pp0} h'(V_{pp0})}{\sigma_{Vs}} \tag{4}$$

where σ_{Vs} is the standard deviation of the baseline. Since the running buffer and the stimulus (sample injected) are held constant, A, Y_0, and ΔY are constant. Thus, one may optimize the detection performance by maximizing the following function:

$$\gamma(V_{pp0}) = \frac{V_{pp0} h'(V_{pp0})}{\sigma_{Vs}} \tag{5}$$

The function h was evaluated at some frequencies by acquiring V_{dc} at different values of V_{pp}. The result is shown in Fig. 8. At 400 kHz, a linear range is

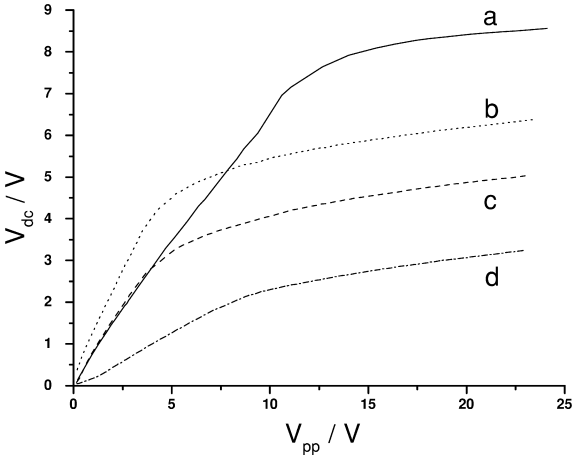

Fig. 8. V_{dc} as a function of V_{pp} (function h) at various operating frequencies: (A) 400 kHz, (B) 590 kHz, (C) 700 kHz, and (D) 900 kHz. Conditions: 75 μm I.D.×360 μm O.D. fused-silica capillary filled with 20 mM Lac/His running buffer.

observed up to ~10 V. The linear range is drastically reduced at 590 kHz. However, this does not mean that the lower frequency is necessarily the best choice, because the derivative of the curve is also important (see Eq. (5)), as well as the noise and the contribution of the solution conductivity to the cell admittance. Thus, the results of Eq. (5) in an optimization procedure are rigorously valid for a predetermined frequency only. However, for two near values of frequency, it is possible in some cases to compare the γ values.

Taking into account the results from Table 1, one can observe that the S/N is correlated to the γ values. Of course, the same γ value yields different S/N for different species. However, it is possible to normalize the response so that the data from different species can be pooled, yielding an average value. Thus, a unique value is obtained for each line of Table 1. The pooled coefficient of correlation is 0.998 with 4 df which validates the use of the γ function as a good estimate for the S/N based on a confidence level of 95%.

Operating frequency optimization is more complicated than amplitude optimization, as mentioned earlier. However, a relatively simple approach can be used to find the maximum frequency to be considered. If a low value of V_{pp} is used, it is possible to establish the linear range for an extended frequency range. Thus, the h function would be represented by straight lines with different slopes for different frequencies. From Fig. 8 and Eq. (3), one can observe that in this case the greater the baseline (V_{dc}), the greater the peaks (V_s) would be. Thus, as an initial approximation, one could consider the baseline intensity as an estimator of the peak height.

Table 1
γ Function and S/N

Frequency (kHz)	V_{pp}/V	γ	S/N[a]			
			K^+	Ba^{2+}	Na^+	Li^+
400	0.5	71	14	16	11	9
400	3.0	556	89	117	87	50
400	6.0	1117	175	227	167	102
590	0.5	132	23	28	25	16
590	3.0	659	135	168	119	71
590	6.0	447	75	100	73	45

[a] Signal-to-noise ratio is based on the peak heights and standard deviation of the baseline.

Table 2
Baseline and peak heights

Frequency (kHz)	V_{dc}/V	Peak height (V_s)/V		
		Sulfate	Methane-sulfonate	Lactate
500	1.816	1.362	0.486	0.321
520	1.916	1.454	0.533	0.351
550	2.126	1.479	0.529	0.344
560	2.205	1.509	0.541	0.360
570	2.261	1.556	0.568	0.374
580	2.300	1.525	0.552	0.362
588	2.306	1.443	0.522	0.331
600	2.288	1.487	0.536	0.346
610	2.249	1.501	0.541	0.358
620	2.192	1.449	0.532	0.345
650	1.980	1.304	0.471	0.312

Electrokinetic injection at 5 kV for 5 s; applied potential −20 kV.

Indeed, Table 2 shows the values of the baseline and peak heights for electropherograms of sulfate, methanesulfonate, and lactate at different operating frequencies and holding a constant V_{pp}. The pooled coefficient of correlation is 0.668 with 9 df, which validates this approach based on a confidence level of 95%. It is worthwhile to note that this approach does not optimize S/N, but peak height. Moreover, there is a dynamic limitation at high frequencies. Thus, if low V_{pp} is used in this screening, the frequency found for the maximum baseline is the limiting frequency, i.e. the best operating frequency certainly will be below it. This procedure does not allow a precise and complete frequency optimization, but works as a fast screening tool, which is useful as an initial step.

Following the above considerations, one can optimize the detection system by tracking the following steps. First, the buffer system is chosen on the basis of the suitability to the analyte separation and conductometric detection. Next, the capillary should be filled with the running buffer and an initial operating frequency is established by maximizing the baseline at low V_{pp}. Because of the limitation of the electronics, the best operating frequency will be less than or equal to this frequency. Next, at the selected frequency, V_{dc} should be acquired at various values of V_{pp}. It is possible to estimate the product $V_{pp}h'(V_{pp})$ numerically from these data. By maximizing this product, one would be maximizing the

function γ for a homoscedastic case, i.e. the noise is independent of the V_{pp}. The next step is to evaluate the noise at some frequencies corresponding to the top of the function, in order to prevent the effect of the data heteroscedasticity. The procedure should be carried out again at a new operating frequency before the final decision is made as to how the amplitude and frequency will be used in the real sample analyses.

It is worth noting that the operating frequency screening and the V_{pp} optimization as proposed above can be instrumentally implemented in such a way that a fast and operator-free optimization routine can be established.

4. Conclusions

The new version of the contactless conductivity detector described here is smaller and easier to operate than the former. Under the experimental conditions employed in this work, the detector can be placed at the low- or high-voltage end of the column.

Amplitude and frequency of the input signal should be optimized for each column diameter and running buffer. As a rule of thumb, high frequency gives the best sensitivity, because the silica wall impedance is reduced. However, the electronics impose limitations. Because the circuit is sensitive to the input current, if a high-conductivity running buffer is used, module 1 may start to operate at a non-ideal condition. Thus, the amplitude and/or frequency should be reduced to improve the sensitivity.

Baseline monitoring at low V_{pp} allows one to find the maximum operating frequency. Function γ can be used for the amplitude optimization procedure at a fixed frequency. Both procedures are advantageous because no sample injection is required.

Acknowledgements

This work was supported by the Conselho Nacional de Desenvolvimento Cientifico e Tecnológico (CNPq) and Fundação de Amparo à Pesquisa do Estado de São Paulo (FAPESP).

References

[1] F.E.P. Mikkers, F.M. Everaerts, Th.P.E.M. Verheggen, J. Chromatogr. 169 (1979) 11.
[2] X. Huang, T.-K.J. Pang, M.J. Gordon, R.N. Zare, Anal. Chem. 59 (1987) 2747.
[3] C. Haber, W.R. Jones, J. Soglia, M. Surve, M. McGlynn, A. Caplan, J.R. Reineck, C. Krstanovic, J. Capillary Electrophor. 3 (1996) 1.
[4] W.R. Jones, J. Soglia, M. McGlynn, C. Haber, J. Reineck, C. Krstanovic, Am. Lab. March (1996) 25.
[5] C.W. Klampfl, J. Agric. Food Chem. 47 (1999) 987.
[6] C.W. Klampfl, M.U. Katzmayr, J. Chromatogr. A 822 (1998) 117.
[7] C.W. Klampfl, M.U. Katzmayr, W. Buchberger, Electrophoresis 19 (1998) 2459.
[8] T.E. Rosso, P.C. Bossle, J. Chromatogr. A 824 (1998) 125.
[9] A.F. Nassar, S.V. Lucas, W.R. Jones, L.D. Hoffland, Anal. Chem. 70 (1998) 1085.
[10] S. Valsecchi, G. Tartan, S. Polesello, J. Chromatogr. A 760 (1997) 326.
[11] D. Kaniansky, V. Zelenská, D. Baluchová, Electrophoresis 17 (1996) 1890.
[12] F. Hissner, J. Mattusch, K. Heinig, J. Chromatogr. A 848 (1999) 503.
[13] D. Schlegel, J. Mattusch, R. Wennrich, Fresenius J. Anal. Chem. 354 (1996) 535.
[14] C.W. Klampfl, M.U. Katzmayr, W. Buchberger, J. High Resolut. Chromatogr. 22 (1999) 297.
[15] C.W. Klampfl, J. Capillary Electrophor. 5 (1998) 125.
[16] C.W. Klampfl, M.U. Katzmayr, W. Buchberger, N. Basener, J. Chromatogr. A 804 (1998) 357.
[17] Th. Meissner, F. Eisenbeiss, B. Jastorff, J. Chromatogr. A 829 (1998) 351.
[18] C. Haber, R.J. VanSaun, Anal. Chem. 70 (1998) 2261.
[19] D. Kaniansky, I. Zelenský, A. Hybenová, F.I. Onuska, Anal. Chem. 66 (1994) 4258.
[20] P.A. Gallagher, C.M. Gertel, N.D. Danielson, J. Chromatogr. A 817 (1998) 31.
[21] P.A. Gallagher, N.D. Danielson, J. Chromatogr. A 781 (1997) 533.
[22] F. Hißner, J. Mattusch, K. Heinig, Fresenius J. Anal. Chem. 365 (1999) 647.
[23] K. Govindaraju, E.A. Cowley, D.H. Eidelman, D.K. Lloyd, Anal. Chem. 69 (1997) 2793.
[24] R.C. Williams, R.J. Boucher, J. Pharm. Biomed. Anal. 22 (2000) 115.
[25] C.J. Stocking, J.M. Slater, R. Unwin, S. Walter, E. Folkerd, Kidney Int. 56 (1999) 338.
[26] S. Fu, C.A. Lucy, Anal. Chem. 70 (1998) 173.
[27] K. Govindaraju, A. Ahmed, D.K. Lloyd, J. Chromatogr. A 768 (1997) 3.
[28] N. Avdalovic, C.A. Pohl, R.D. Rocklin, J.R. Stillian, Anal. Chem. 65 (1993) 1470.
[29] P.K. Dasgupta, L. Bao, Anal. Chem. 65 (1993) 1003.
[30] P.K. Dasgupta, S. Kar, Anal. Chem. 67 (1995) 3853.

[31] M. Harrod, J. Stillian, L. Bao, R. Rocklin, N. Avdalovic, J. Chromatogr. A 717 (1995) 371.
[32] H. Zhao, R. Dadoo, R.J. Reay, G.T.A. Kovacs, R.N. Zare, J. Chromatogr. A 813 (1998) 205.
[33] D. Müller, J. Jelínek, F. Opekar, K. Stulík, Electroanalysis 8 (1996) 722.
[34] S. Kar, P.K. Dasgupta, H. Liu, H. Hwang, Anal. Chem. 66 (1994) 2537.
[35] P. Tuma, F. Opekar, I. Jenelík, K. Stulík, Electroanalysis 11 (1999) 1022.
[36] M.U. Katzmayr, C.W. Klampfl, W. Buchberger, J. Chromatogr. A 850 (1999) 355.
[37] C.A. Lucy, Q. Wu, J. Chromatogr. Sci. 36 (1998) 33.
[38] P. Gebauer, J. Caslavska, W. Thormann, P. Bocek, J. Chromatogr. A 772 (1997) 63.
[39] A.J. Zemann, E. Schnell, D. Volgger, G.K. Bonn, Anal. Chem. 70 (1998) 563.
[40] J.A.F. Silva, C.L. Lago, Anal. Chem. 70 (1998) 4339.
[41] K. Mayrhofer, A.J. Zemann, E. Schnell, G.K. Bonn, Anal. Chem. 71 (1999) 3828.
[42] B. Gas, M. Demjanenko, J. Vacík, J. Chromatogr. 192 (1980) 253.
[43] J. Vacík, J. Zuska, I. Muselasová, J. Chromatogr. 320 (1985) 233.
[44] D. Kaniansky, V. Zelenská, M. Masár, F. Iványi, S. Gazdíková, J. Chromatogr. A 844 (1999) 349.
[45] M. Masár, R. Bodor, D. Kaniansky, J. Chromatogr. A 834 (1999) 179.
[46] P. Mikus, D. Kaniansky, R. Sebesta, M. Salisová, Enantiomer 4 (1999) 279.
[47] J.A.F. Silva, C.L. Lago, Electrophoresis 21 (2000) 1405.
[48] T. Chvojka, I. Jelínek, F. Opekar, K. Štulík, Anal. Chim. Acta 433 (2001) 13.
[49] I. Fanderlik (Ed.), Silica Glass and Its Application, Glass Science and Technology, Vol. 11, Elsevier, Amsterdam, 1991, p. 240, Chapter 4.